Journal of the European Ceramic Society 43 (2023) 4581–4587

Contents lists available at ScienceDirect

Journal of the European Ceramic Society

journal homepage: www.elsevier.com/locate/jeurceramsoc

Original article

Thermal and ablation properties of a high-entropy metal diboride: $(Hf_{0.2}Zr_{0.2}Ti_{0.2}Ta_{0.2}Nb_{0.2})B_2$

Md Shafkat Bin Hoque [a], Milena Milich [a], Md Sabbir Akhanda [b], Sashank Shivakumar [c], Eric R. Hoglund [d], Dragos Staicu [e], Mingde Qin [c], Kathleen F. Quiambao-Tomko [d], John A. Tomko [a], Jeffrey L. Braun [f], Joshua Gild [c], David H. Olson [f], Kiumars Aryana [a], Yee Rui Koh [a], Roisul Galib [a], Luka Vlahovic [e], Davide Robba [e], John T. Gaskins [f], Mona Zebarjadi [b], Jian Luo [c], Patrick E. Hopkins [a,d,g,*]

[a] Department of Mechanical and Aerospace Engineering, University of Virginia, Charlottesville, VA 22904, USA
[b] Department of Electrical Engineering, University of Virginia, Charlottesville, VA 22904, USA
[c] Materials Science and Engineering Program, University of California San Diego, La Jolla, CA, 92093, USA
[d] Department of Materials Science and Engineering, University of Virginia, Charlottesville, VA 22904, USA
[e] European Commission, Joint Research Centre, Institute for Transuranium Elements, P.O. Box 2340, D-76125 Karlsruhe, Germany
[f] Laser Thermal Analysis, Charlottesville, VA 22902, USA
[g] Department of Physics, University of Virginia, Charlottesville, VA 22904, USA

ARTICLE INFO

Keywords:
High-entropy metal diboride
Thermal properties
Ablation resistance

ABSTRACT

The fabrication of high-entropy ceramics has recently expanded the pool of ultra-high temperature ceramics (UHTCs). To properly assess the suitability of these new types of ceramics for advanced aerospace applications, it is of vital interest to extend the characterizations beyond ambient conditions. Here, we have studied the thermal and ablation properties of a high-entropy diboride (HEB): $(Hf_{0.2}Zr_{0.2}Ti_{0.2}Ta_{0.2}Nb_{0.2})B_2$. The thermal conductivity of the HEB increases as a function of temperature and becomes comparable to that of other UHTCs at high temperatures. The electron dominated thermal conductivity of HEB is also nearly isotropic along different crystallographic orientations. The temperature-dependent volumetric heat capacity of HEB is measured and found to remain in agreement with that of ZrB_2. Additionally, both material systems possess nearly the same ablation resistance. The multitudes of characterizations performed in this study establishes the suitability of HEB for high thermal load applications in extreme environments.

1. Introduction

High-entropy ceramics have garnered a lot of attention in recent years due to their unique mechanical, physical, and thermal characteristics [1–3]. Typically in a high-entropy ceramic, five or more components are mixed in equimolar or near-equimolar concentrations to maximize the configuration entropy and minimize the Gibbs free energy [4–8]. The minimization of Gibbs free energy leads to higher thermodynamic stability, making high-entropy ceramics promising for a wide array of applications. To date, different types of high-entropy ceramics, such as metal diborides [9,10], metal carbides [11–16], nitrides [6,17], sulfides [18], silicides [19,20], fluorites [21,22] and oxides [23–29], have been successfully fabricated.

Among different classes of high-entropy ceramics, metal diborides and carbides fall into the category of ultra-high temperature ceramics (UHTCs), i.e., materials suitable for extreme environment applications such as next generation gas turbines, rocket nozzles, and scramjet propulsion [30]. Prior to the successful fabrication of high-entropy metal diborides and carbides, the pool of UHTCs were mostly limited to monolithic binary borides and carbides. Several of them, such as ZrB_2, ZrC, HfB_2, and HfC, have been studied for decades for advanced aerospace applications [31,32]. However, the diverse demands of the aerospace, energy, and nuclear industries have made it a necessity to expand the pool of UHTCs and characterize their properties [33].

Thus far, the vast majority of the characterizations performed on high-entropy metal diborides and carbides have focused on room-temperature thermal and mechanical properties [34,35]. To properly assess the suitability of high-entropy metal diborides and carbides for extreme environment applications, it is necessary to extend the characterizations beyond ambient conditions. Towards this goal, we have performed a series of thermal and ablation characterizations on a single-phase high-entropy diboride (HEB) in this work. The composition of the studied HEB is $(Hf_{0.2}Zr_{0.2}Ti_{0.2}Ta_{0.2}Nb_{0.2})B_2$.

* Corresponding author.
E-mail address: phopkins@virginia.edu (P.E. Hopkins).

https://doi.org/10.1016/j.jeurceramsoc.2023.03.065
Received 15 December 2022; Received in revised form 20 March 2023; Accepted 30 March 2023
Available online 5 April 2023
0955-2219/© 2023 Published by Elsevier Ltd.

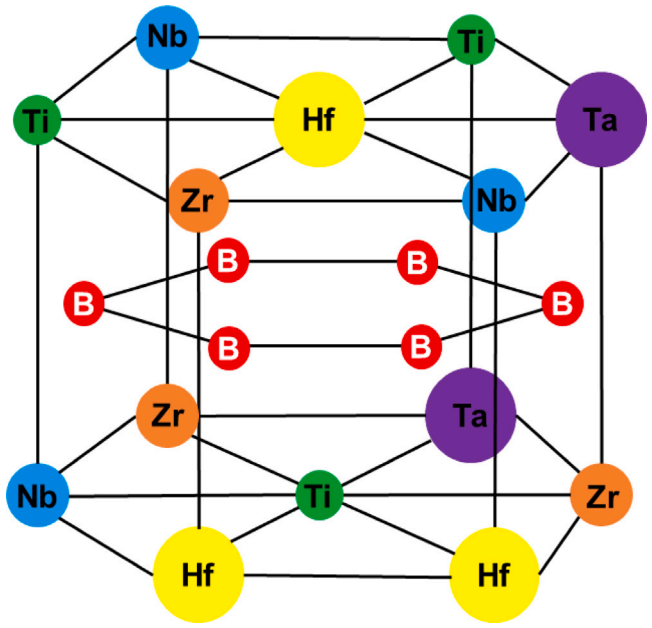

Fig. 1. Schematic diagram of the crystal structure of $(Hf_{0.2}Zr_{0.2}Ti_{0.2}Ta_{0.2}Nb_{0.2})B_2$. *Source:* Taken and modified from Gild et al. [9].

We provide the first detailed thermal characterizations of a HEB. Our four-point probe characterization reveals that the thermal conductivity of the HEB is electron dominated. We next measure the thermal conductivity of HEB up to 1267 °C. Due to electron-dominated thermal transport, the thermal conductivity of HEB increases as a function of temperature. Such increasing thermal conductivity trend is highly promising for avoiding failure due to thermal shock at high temperatures. We additionally measured room temperature thermal conductivity maps on HEB and found that the HEB possesses a nearly isotropic thermal conductivity contrary to that of monolithic metal diborides, such as ZrB_2 [36,37]. The temperature-dependent volumetric heat capacity of HEB is measured and found to remain in agreement with that of ZrB_2.

Along with the thermal properties of the HEB, we study its ablation resistance. At high temperatures, materials can also erode via ablation, which is controlled by a combination of thermomechanical, thermochemical, and thermophysical processes [38–41]. Therefore, the ablation resistance characterization provides a suitable gauge for determining the onset of any high thermal-load induced failure in a material. Our ablation threshold measurements reveal that the ablation resistance of the HEB is nearly the same as that of ZrB_2. The thermal and ablation characterizations performed in this study are beneficial for assessing the suitability of HEB for extreme structural and hypersonic applications.

2. Microstructural details of the HEB specimen

The HEB studied in this work possesses a single-phase, hexagonal crystal structure (AlB_2) [42] with high symmetry [9,19]. Fig. 1 shows the highly anisotropic layered crystal structure of the HEB consisting of alternating rigid two-dimensional (2D) boron nets and 2D layers of five metal cations (Hf, Zr, Ti, Ta, and Nb) [9]. The polycrystalline HEB sample for this study was fabricated by reactive spark plasma sintering of ball milled elemental powders [43]. During spark plasma sintering, the powders were first held at temperatures of 1400 and 1600 °C for 80 min each to allow for sufficient outgassing and native oxide reduction. The temperature was then raised at 30 °C/min to the final sintering temperature of 2200 °C and held for 30 min, prior to cooling to room temperature in 15–20 min. A pressure of 80 MPa was applied at the maximum temperature to enable full densification. The prepared specimen was highly dense (> 98% of theoretical density) and contained negligible amount of native oxide contaminants. The composition of the sample was measured by energy dispersive X-ray spectroscopy (EDS) to be 98% $(Hf_{0.19}Zr_{0.19}Ti_{0.22}Ta_{0.19}Nb_{0.18}W_{0.03})B_2$ with residual amount of carbide phase [43]. The average grain size of the HEB specimen was 15±9.5 μm, as measured by electron backscatter diffraction (EBSD). A detailed description of the HEB sample fabrication and characterization can be found in Qin et al. [43] The HEB specimen of this study and that of Ref. [43] were prepared following the same methodology.

Table 1
Thermal conductivity, relative density, and volumetric heat capacity of the HEB specimen measured in this study. For comparison, we also include the relevant properties of the constituent metal diborides from the literature. The thermal conductivity of high-quality TaB_2 has not been previously reported in the literature.

Materials	Thermal conductivity (W m^{-1} K^{-1})	Relative density	Volumetric heat capacity (MJ m^{-3} K^{-1})
$(Hf_{0.2}Zr_{0.2}Ti_{0.2}Ta_{0.2}Nb_{0.2})B_2$	27.8 ± 2.9	> 98	2.84 ± 0.34
HfB_2	107 [60]	96	2.81 [61,62]
ZrB_2	127 [37]	99.5	2.95 [37]
TiB_2	96 [63]	99.5	2.84 [61]
TaB_2	–	–	3.05 [61]
NbB_2	102 [64]	> 97	2.91 [61,65]

3. Results and discussion

3.1. Thermal conductivity of the HEB

To measure the thermal conductivity of the HEB, we employed three different thermal characterization techniques: steady-state thermoreflectance (SSTR) [44], time-domain thermoreflectance (TDTR) [45–48], and laser flash analysis (LFA) [49]. SSTR and TDTR are used to measure the thermal conductivity up to 290 and 600 °C, respectively. LFA is used to measure thermal diffusivity up to 1267 °C from which we extract the thermal conductivity. Although SSTR can measure the thermal conductivity independent of heat capacity, TDTR and LFA measurements require knowledge of HEB heat capacity [50–52]. To this end, we assumed that the heat capacity of the HEB and ZrB_2 is the same. This assumption is later verified in subsequent sections. Details of the thermal characterization techniques can be found in the Supporting Information.

The room-temperature thermal conductivity of the HEB sample is 27.8 ± 2.9 W m^{-1} K^{-1}. This is in agreement with our previous publications [10,43]. As exhibited in Table 1, the thermal conductivity of the HEB is significantly lower compared to the monolithic diborides of similar relative densities. Both electrons and phonons contribute to the thermal conductivity of these diborides [42,53–55]. A small amount of impurities can reduce the thermal conductivity of the monolithic diborides significantly [56,57]. However, we attribute the thermal conductivity reduction in HEB to the significant electron and phonon scattering caused by the lattice distortions and compositional disorder [3,58]. The localized mass and interatomic bond strength differences among the five metal cations in the HEB cause lattice distortions as evident by the changes in lattice parameters compared to the single diboride counterparts [3,9,11,19]. In addition, the 2D rigid boron nets highly strain the metal–metal bonding within the 2D cation layers leading to further electron and phonon scattering [9]. Due to such extensive nature of electron and phonon scattering, the presence of small impurities (i.e., tungsten or the carbide phase) is not expected to cause a significant reduction in HEB thermal conductivity [43,59].

To approximate the electron contribution (κ_e) to the thermal conductivity of the HEB, we use the Wiedemann–Franz law: $\kappa_e = \sigma_e LT$,

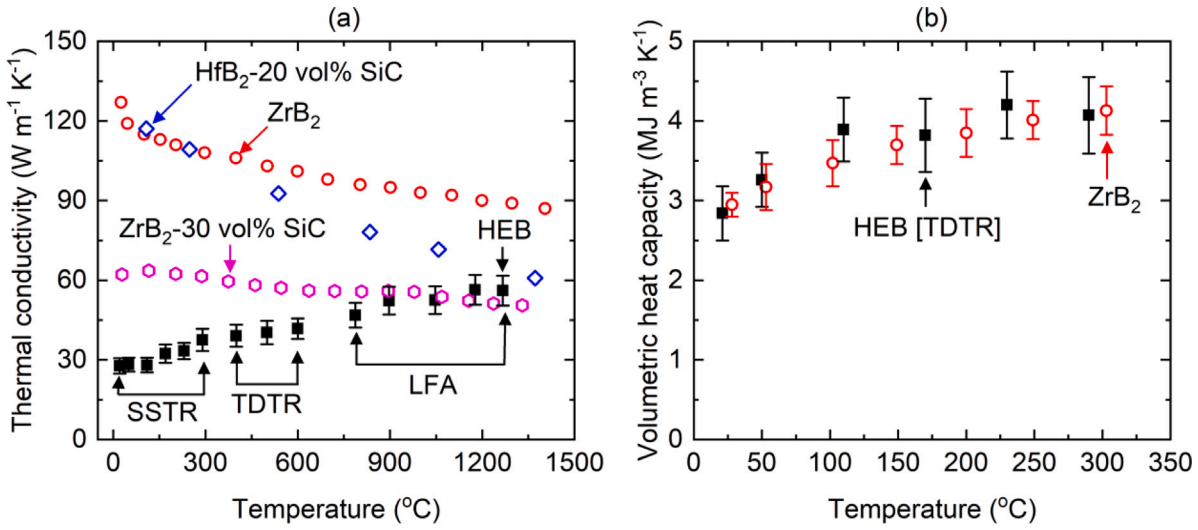

Fig. 2. (a) Temperature-dependent thermal conductivity of HEB measured via three different techniques: SSTR (21–290 °C), TDTR (400–600 °C), and LFA (787–1267 °C). For comparison, we also include the thermal conductivity of ZrB_2 [37], ZrB_2-30 vol% SiC [55], and HfB_2-20 vol% SiC [60] from literature. (b) Temperature-dependent heat capacity of HEB along with that of ZrB_2 [37].

where σ_e, L, and T represent electrical conductivity, Lorentz number, and temperature, respectively [55]. For this purpose, we measure the electrical conductivity via the four-point probe method and use a Lorentz number of 2.45×10^{-8} W Ω K^{-2}. This ideal Lorentz number has been previously used to estimate the κ_e values of ZrB_2 [66], HfB_2 [67], ZrB_2-TiB_2 [66], and ZrB_2-SiC [55] ceramics. The measured electrical conductivity of the HEB specimen is $(2.42 \pm 0.12) \times 10^6$ S/m. This value corresponds to an electron contribution of 18.1 ± 0.9 W m^{-1} K^{-1}, nearly 65% of the total thermal conductivity of HEB. Thus, our measurement provides the first empirical evidence that the thermal conductivity of HEB is electron dominated.

The temperature-dependent thermal conductivity of the HEB specimen is presented in Fig. 2(a). For comparison, we also include the thermal conductivity of several traditional UHTCs such as ZrB_2 [37], ZrB_2-30 vol% SiC [55], and HfB_2-20 vol% SiC [60]. As evident here, at room temperature, the thermal conductivity of these ceramics is significantly higher than that of the HEB. However, as temperature increases, the thermal conductivity of HEB, ZrB_2, ZrB_2-30 vol% SiC, and HfB_2-20 vol% SiC ceramics starts to converge. The increase in thermal conductivity of the HEB with temperature can be attributed to its electron dominated thermal transport [66]. This trend provides optimism that at elevated temperatures (i.e., > 2000 °C), the thermal conductivity of HEB can become comparable to or even higher than that of other UHTCs. At such temperatures, high thermal conductivity is desired of UHTCs to avoid failure due to thermal shock [30,57,60]. Therefore, the thermal conductivity measurements show that the HEB is a promising material for extreme environment applications such as hypersonic aerospace vehicles.

3.2. Volumetric heat capacity of the HEB

Using the SSTR-measured thermal conductivity as an input parameter, we extract the volumetric heat capacity of HEB from TDTR measurements up to 290 °C. The room-temperature heat capacity of the HEB specimen is presented in Table 1. As exhibited here, the heat capacity of HEB is nearly the same as that of the constituent diborides. Furthermore, this value is in agreement with the rule of mixture [68] prediction (2.91 MJ m^{-3} K^{-1}). The temperature-dependent heat capacity of the HEB specimen is presented in Fig. 2(b). The excellent agreement shown between HEB and ZrB_2 supports our earlier assumption that the volumetric heat capacities of the two materials are nearly identical.

3.3. Spatial thermal conductivity mapping of HEB and ZrB_2

To investigate the presence of any anisotropy in the thermal conductivity of HEB, we spatially mapped the HEB specimen using TDTR. For comparison, we also spatially mapped the thermal conductivity of a reference ZrB_2 system. The ZrB_2 specimen used for this purpose was prepared by reactive hot pressing and had a relative density > 96% [37,57]. EDS technique reveals the presence of 92–93 wt% zirconium in the ZrB_2 specimen. The sample also contains oxygen, magnesium, titanium, and strontium impurities, and has an average grain size of 7.3 ± 4.2 μm. Therefore, we used a probe spot size ($1/e^2$ diameter) of 6 μm or less and a modulation frequency of 8.4 MHz for TDTR mapping to ensure that the thermal penetration depth (< 1.5 μm) remains lower than the HEB and ZrB_2 grain sizes [51]. At such low thermal penetration depth, TDTR mapping is a good indicator of the cross-plane thermal conductivity of individual grains. To correlate TDTR mapping with grain orientations, we performed EBSD characterization of the samples. Details of our TDTR mapping, EDS, and EBSD characterizations have been provided in the Supporting Information and previous works [69,70].

Fig. 3(a_1) and (a_2) show the EBSD micrographs of the HEB and ZrB_2 specimens, respectively. The HEB grains are randomly oriented without any significant texturing. In contrast, the ZrB_2 grains are preferentially oriented along the 001 direction. The difference in texturing between the HEB and ZrB_2 can be attributed to the different fabrication techniques of the two specimens [71,72].

As TDTR measures the thermal conductivity along the cross-plane direction, we used the pole figures to confirm the distribution of 001 oriented grains along the Z-axis. Fig. 3(b_1) indicates that the 001 oriented grains are randomly distributed along the Z-axis in the HEB. In contrast, Fig. 3(b_2) shows that the intensity of 001 oriented grains is highest along the Z-axis in ZrB_2.

Fig. 3(c_1) and (c_2) show the disorientation angle distributions of HEB and ZrB_2, respectively. For comparison, we also show the corresponding Mackenzie distribution, i.e., the theoretical distribution of a randomly oriented polycrystalline material of hexagonal crystal structure. The disorientation angle distribution for HEB largely follows the ideal Mackenzie distribution, confirming that the grains are randomly oriented. For ZrB_2, there is an increased proportion of smaller disorientation angles compared to that of a random distribution, indicating the presence of texturing.

The cross-plane thermal conductivity distributions of HEB and ZrB_2 are presented in Fig. 3(d_1) and (d_2), respectively. The thermal conductivity maps used to extract the distributions are provided in the

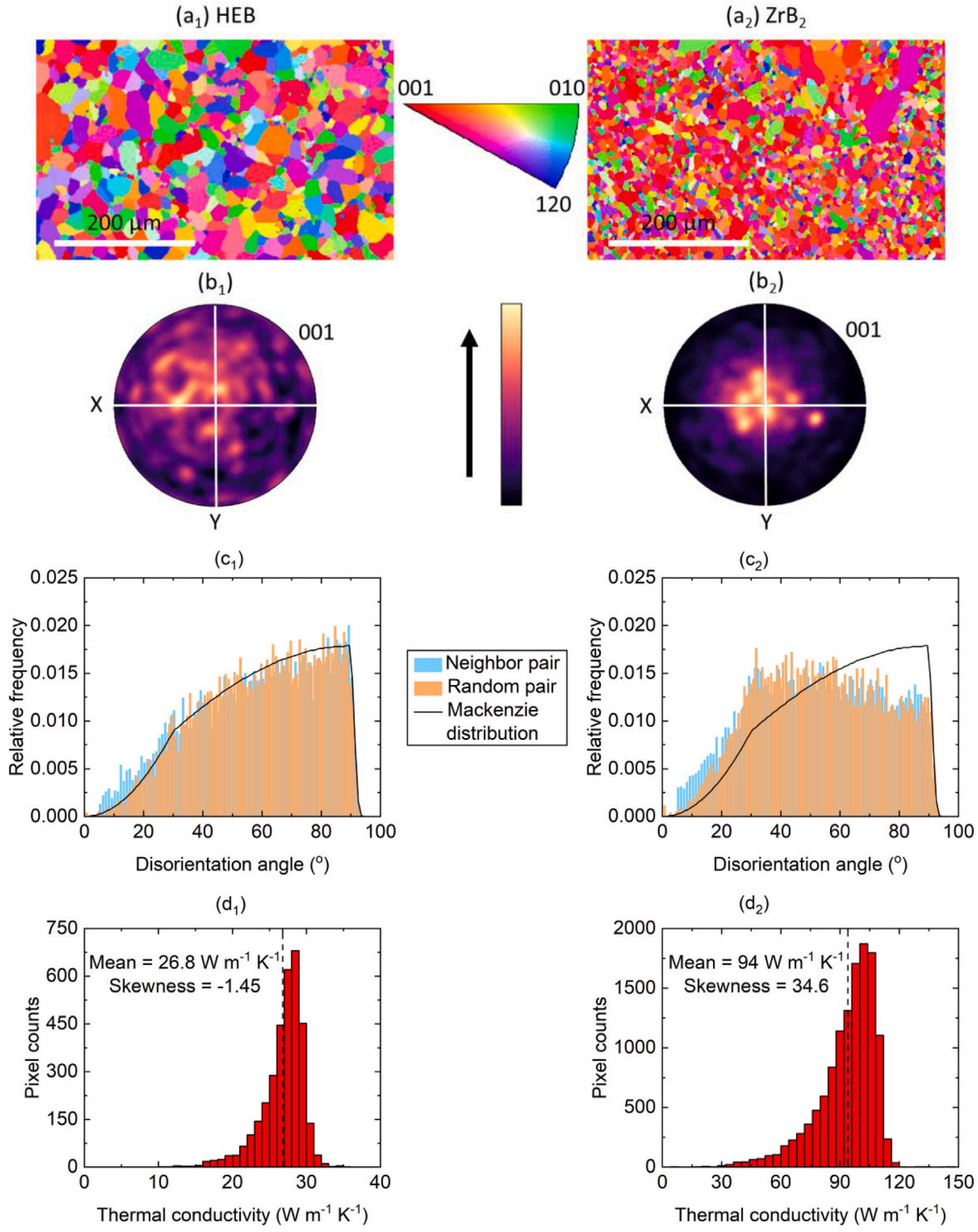

Fig. 3. [a_1, a_2] EBSD micrographs exhibiting the grain orientations in HEB and ZrB_2. [b_1, b_2] Pole figures exhibiting the distribution of 001 oriented grains along the *Z*-axis. [c_1, c_2] Disorientation angle distributions extracted from the EBSD data. [d_1, d_2] Thermal conductivity distributions extracted from TDTR mapping. Subscript 1 and 2 denote HEB and ZrB_2, respectively.

Supporting Information. As exhibited in Fig. 3(d_1), the thermal conductivity of HEB is relatively symmetric around the mean value. Nearly 89% of the pixel counts can be found within just ~15% of the mean value. The results are confirmed in multiple thermal conductivity maps on different regions of the HEB specimen. The lower thermal conductivity pixel counts of Fig. 3(d_1) likely stem from impurities such as the carbide phase. Due to the presence of such impurities, the HEB thermal conductivity distribution has a skewness value less than −1. For comparison, the thermal conductivity distribution of ZrB_2 is nearly 24 times more skewed. This can be attributed to the higher impurity concentrations of the ZrB_2 specimen. The 001 oriented grains of ZrB_2 can possess thermal conductivities ranging from 95 to 102 W m^{-1}

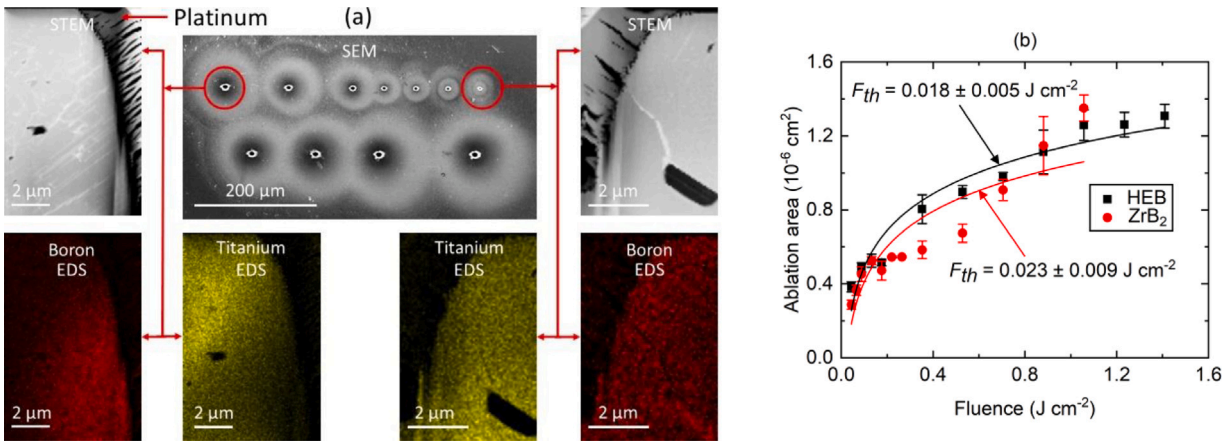

Fig. 4. (a) SEM, STEM, and EDS images of the ablation areas on the HEB sample surface. The left and right panels represent the left and right half of the near-symmetric holes, respectively. (b) Ablation areas as a function of incident laser fluences for the HEB and ZrB_2 specimens.

K^{-1}, whereas grains oriented along other crystallographic directions can have a thermal conductivity above 120 W m^{-1} K^{-1} [36,37]. The absence of pixel counts with thermal conductivities above 120 W m^{-1} K^{-1} shows that the mean thermal conductivity of Fig. 3(d_2) is representative of ZrB_2 textured along the 001 crystallographic direction.

The relatively symmetric distribution and similar thermal conductivity maps on multiple regions of the HEB specimen reveal that the thermal conductivity of HEB is nearly isotropic across different crystallographic orientations. Therefore, the temperature-dependent thermal conductivity values exhibited in Fig. 2(a) is representative of HEB textured in any orientation. However, we note that even for materials with anisotropic thermal conductivity, such as ZrB_2, the effect of anisotropy is likely to be very small at high temperatures [37,57].

3.4. Ablation resistance of HEB and ZrB_2

The thermal characterizations of the HEB suggests that it could be used as a suitable material in extreme environments in lieu of metal diborides. Therefore, to assess the performance of the HEB under extreme thermal loads, we studied the ablation resistance of the HEB and ZrB_2 specimens. For this purpose, we performed laser ablation threshold measurements on both materials. In our laser ablation setup, a sub-picosecond, 520 nm laser is focused onto the sample surface with varying pulsed fluences. We report the threshold for 1200 pulses incident upon the sample to eliminate the role of surface inhomogeneities that may alter the optical absorption of single pulse measurements [73,74]. Additional details regarding the ablation setup are provided in the Supporting Information.

The central panel of Fig. 4(a) shows a secondary electron image of a series of ablated regions on the HEB sample surface corresponding to varying laser fluences. The diameter of each area is measured using a standard optical microscope as well as a scanning electron microscope (SEM); the two methods are found to be in good agreement. A small and a medium size hole are selected from the ablated regions for higher resolution analysis using scanning transmission electron microscopy (STEM). The diffraction contrast images show a clear difference in defect microstructures induced by variable laser fluences. When the laser fluence is low and hole size is small, no noticeable plastic deformation is noticed in the right panel figure. The bright grain boundary with the BN precipitate may have been present prior to ablation. On the other hand, when the hole size is medium, planar defects propagate from the ablated region into the bulk as shown in the left panel figure. The difference between the left and right panel figures shows how the material transitions to accommodate the absorbed energy. EDS maps reveal that the boron composition is uniform when the laser fluence is low, but when laser fluence is medium, there is boron enrichment and titanium depletion in plastically deformed region. Supporting Information Figure S5 shows that the intensity in the atomic number contrast images is relatively flat, thus indicating that the mass density is well balanced between elemental species and the sample is uniform in thickness. Additional EDS maps further indicate that the plastically deformed region is rich in boron and niobium while depleted in zirconium, titanium, tantalum, and hafnium.

In Fig. 4(b), the ablation areas as a function of incident laser fluences for both the HEB and ZrB_2 samples are reported. To extract the onset of material failure, i.e., the ablation threshold, F_{th}, we fit the following equation [75,76] to our experimental data

$$D^2 = 2\omega_o^2 ln\frac{F}{F_{th}} \quad (1)$$

where D is the diameter of the ablation region, ω_o is the beam waist of the laser, and F is the incident fluence. Due to the short pulse duration used here (~200 fs), the ablation threshold is dictated by the atomic bonding energy of the material with minimal contributions from thermal diffusion into the surrounding region [76,77].

As exhibited in Fig. 4(b), the ablation thresholds of HEB and ZrB_2 are measured to be 0.018 ± 0.005 and 0.023 ± 0.009 J cm^{-2}, respectively; nearly the same within uncertainty. This indicates that the HEB and ZrB_2 possess very similar bond strengths and hence, nearly-identical thermal ablation resistances. To further verify this, we compare the elastic modulus of the two materials as it is also an indicator of bond strength [3,78]. Qin et al. [43] recently reported the elastic modulus of the HEB to be ~525 GPa. Using nanoindentation [79,80], we measure the elastic modulus of the ZrB_2 specimen to be 502 ± 30 GPa. In short, through a combination of laser-induced ablation measurements and nanoindentation, our results strongly suggest that the HEB studied in this work has very similar mechanical properties to those of ZrB_2. We note that this conclusion may change based on the relative density and purity level of the HEB or ZrB_2 specimen [81]. As ZrB_2 is widely regarded as a promising material for high temperature structural applications [42,66,82], our measurements potentially suggest that highly dense HEB may be a strong competing material candidate for similar applications.

4. Conclusions

The thermal and ablation properties of a HEB are presented in this work. Our study reveals that the electrons contribute to nearly 65% of the total thermal conductivity of HEB. We used multiple thermal characterization techniques to measure the HEB thermal conductivity up to 1267 °C. The comparable thermal conductivity of HEB with that of other UHTCs at such temperatures provides evidence that the HEB can be a promising material for use in hypersonic aerospace vehicles

and advanced rocket nozzles. The HEB also possesses a nearly isotropic thermal conductivity along all crystallographic directions, contrary to that of other binary diborides, such as ZrB_2. The volumetric heat capacities of HEB and ZrB_2 remain nearly the same as a function of temperature. We further found that the HEB and ZrB_2 possess nearly identical ablation resistance. The characterizations performed in this study mark a significant advancement towards employing of HEB for ultra-high temperature applications.

Declaration of competing interest

The authors declare that they have no known competing financial interests or personal relationships that could have appeared to influence the work reported in this paper.

Data availability

The data presented in this study are available from the corresponding author upon reasonable request.

Acknowledgments

We appreciate support from the National Science Foundation, USA, Grant No. 1921973 and the Office of Naval Research, USA, Grant No. N00014-22-1-2139. We thank W. G. Fahrenholtz from Missouri University of Science and Technology, USA for providing us the ZrB_2 specimen. M.Q., S.S., J.G., and J.L. acknowledge support from the UC Irvine MRSEC, Center for Complex and Active Materials, under National Science Foundation (NSF), USA Grant No. DMR-2011967.

Appendix A. Supplementary data

Supplementary material related to this article can be found online at https://doi.org/10.1016/j.jeurceramsoc.2023.03.065.

References

[1] D. Bérardan, S. Franger, D. Dragoe, A.K. Meena, N. Dragoe, Colossal dielectric constant in high entropy oxides, Phys. Status Solidi (RRL)–Rapid Res. Lett. 10 (4) (2016) 328–333.
[2] D. Bérardan, S. Franger, A. Meena, N. Dragoe, Room temperature lithium superionic conductivity in high entropy oxides, J. Mater. Chem. A 4 (24) (2016) 9536–9541.
[3] J.L. Braun, C.M. Rost, M. Lim, A. Giri, D.H. Olson, G.N. Kotsonis, G. Stan, D.W. Brenner, J.-P. Maria, P.E. Hopkins, Charge-induced disorder controls the thermal conductivity of entropy-stabilized oxides, Adv. Mater. 30 (51) (2018) 1805004.
[4] M.-H. Tsai, J.-W. Yeh, High-entropy alloys: a critical review, Mater. Res. Lett. 2 (3) (2014) 107–123.
[5] Y. Zhang, T.T. Zuo, Z. Tang, M.C. Gao, K.A. Dahmen, P.K. Liaw, Z.P. Lu, Microstructures and properties of high-entropy alloys, Prog. Mater. Sci. 61 (2014) 1–93.
[6] T. Jin, X. Sang, R.R. Unocic, R.T. Kinch, X. Liu, J. Hu, H. Liu, S. Dai, Mechanochemical-assisted synthesis of high-entropy metal nitride via a soft urea strategy, Adv. Mater. 30 (23) (2018) 1707512.
[7] T. Zhu, P.M. Litwin, M.G. Rosul, D. Jessup, M.S. Akhanda, F.F. Tonni, S. Krylyuk, A.V. Davydov, P. Reinke, S.J. McDonnell, M. Zebarjadi, Transport properties of few-layer NbSe2: From electronic structure to thermoelectric properties, Mater. Today Phys. 27 (2022) 100789.
[8] M.B. Burkholder, M.M. Rahman, A.C. Reber, A.M. Gaffney, B.F. Gupton, J.R. Monnier, New perspectives and insights into direct epoxidation of propylene using O2 and silver-based catalysts, Appl. Catal. A 650 (2023) 119002.
[9] J. Gild, Y. Zhang, T. Harrington, S. Jiang, T. Hu, M.C. Quinn, W.M. Mellor, N. Zhou, K. Vecchio, J. Luo, High-entropy metal diborides: a new class of high-entropy materials and a new type of ultrahigh temperature ceramics, Sci. Rep. 6 (1) (2016) 1–10.
[10] J. Gild, A. Wright, K. Quiambao-Tomko, M. Qin, J.A. Tomko, M.S. bin Hoque, J.L. Braun, B. Bloomfield, D. Martinez, T. Harrington, K. Vecchio, P.E. Hopkins, J. Luo, Thermal conductivity and hardness of three single-phase high-entropy metal diborides fabricated by borocarbothermal reduction and spark plasma sintering, Ceram. Int. 46 (5) (2020) 6906–6913.
[11] X. Yan, L. Constantin, Y. Lu, J.-F. Silvain, M. Nastasi, B. Cui, (Hf0. 2zr0. 2ta0. 2nb0. 2ti0. 2) C high-entropy ceramics with low thermal conductivity, J. Am. Ceram. Soc. 101 (10) (2018) 4486–4491.
[12] J. Zhou, J. Zhang, F. Zhang, B. Niu, L. Lei, W. Wang, High-entropy carbide: A novel class of multicomponent ceramics, Ceram. Int. 44 (17) (2018) 22014–22018.
[13] P. Sarker, T. Harrington, C. Toher, C. Oses, M. Samiee, J.-P. Maria, D.W. Brenner, K.S. Vecchio, S. Curtarolo, High-entropy high-hardness metal carbides discovered by entropy descriptors, Nature Commun. 9 (1) (2018) 1–10.
[14] E. Castle, T. Csanádi, S. Grasso, J. Dusza, M. Reece, Processing and properties of high-entropy ultra-high temperature carbides, Sci. Rep. 8 (1) (2018) 1–12.
[15] T.J. Harrington, J. Gild, P. Sarker, C. Toher, C.M. Rost, O.F. Dippo, C. McElfresh, K. Kaufmann, E. Marin, L. Borowski, P.E. . Hopkins, J. Luo, S. Curtarolo, D.W. Brenner, K.S. Vecchio, Phase stability and mechanical properties of novel high entropy transition metal carbides, Acta Mater. 166 (2019) 271–280.
[16] M.S. Akhanda, S.E. Rezaei, K. Esfarjani, S. Krylyuk, A.V. Davydov, M. Zebarjadi, Thermomagnetic properties of Bi2Te3 single crystal in the temperature range from 55 K to 380 K, Phys. Rev. Mater. 5 (1) (2021) 015403.
[17] V. Braic, A. Vladescu, M. Balaceanu, C. Luculescu, M. Braic, Nanostructured multi-element (TiZrNbHfTa)N and (TiZrNbHfTa)C hard coatings, Surf. Coat. Technol. 211 (2012) 117–121.
[18] R.-Z. Zhang, F. Gucci, H. Zhu, K. Chen, M.J. Reece, Data-driven design of ecofriendly thermoelectric high-entropy sulfides, Inorg. Chem. 57 (20) (2018) 13027–13033.
[19] J. Gild, J. Braun, K. Kaufmann, E. Marin, T. Harrington, P. Hopkins, K. Vecchio, J. Luo, A high-entropy silicide:(Mo0.2Nb0.2Ta0.2Ti0.2W0.2)Si2, J. Materiomics 5 (3) (2019) 337–343.
[20] Y. Qin, J.-X. Liu, F. Li, X. Wei, H. Wu, G.-J. Zhang, A high entropy silicide by reactive spark plasma sintering, J. Adv. Ceram. 8 (1) (2019) 148–152.
[21] J. Gild, M. Samiee, J.L. Braun, T. Harrington, H. Vega, P.E. Hopkins, K. Vecchio, J. Luo, High-entropy fluorite oxides, J. Eur. Ceram. Soc. 38 (10) (2018) 3578–3584.
[22] D. Song, M. Ryu, J. Kwon, G. Lyu, J. Kim, H.-B. Jeon, T. Song, U. Paik, B.-i. Yang, Y.-G. Jung, Y.-S. Oh, Blocking of radiative thermal conduction in Zn2+-Incorporated high-entropy A2B2O7 fluorite oxides, Ceram. Int. 47 (23) (2021) 33544–33553.
[23] R. Djenadic, A. Sarkar, O. Clemens, C. Loho, M. Botros, V.S. Chakravadhanula, C. Kübel, S.S. Bhattacharya, A.S. Gandhi, H. Hahn, Multicomponent equiatomic rare earth oxides, Mater. Res. Lett. 5 (2) (2017) 102–109.
[24] J. Dąbrowa, M. Stygar, A. Mikuła, A. Knapik, K. Mroczka, W. Tejchman, M. Danielewski, M. Martin, Synthesis and microstructure of the (Co, Cr, Fe, Mn, Ni)3O4 high entropy oxide characterized by spinel structure, Mater. Lett. 216 (2018) 32–36.
[25] S. Jiang, T. Hu, J. Gild, N. Zhou, J. Nie, M. Qin, T. Harrington, K. Vecchio, J. Luo, A new class of high-entropy perovskite oxides, Scr. Mater. 142 (2018) 116–120.
[26] Y. Sharma, B.L. Musico, X. Gao, C. Hua, A.F. May, A. Herklotz, A. Rastogi, D. Mandrus, J. Yan, H.N. Lee, M.F. Chisholm, V. Keppens, T.Z. Ward, Single-crystal high entropy perovskite oxide epitaxial films, Phys. Rev. Mater. 2 (6) (2018) 060404.
[27] D. Vinnik, E. Trofimov, V. Zhivulin, O. Zaitseva, S. Gudkova, A.Y. Starikov, D. Zherebtsov, A. Kirsanova, M. Häßner, R. Niewa, High-entropy oxide phases with magnetoplumbite structure, Ceram. Int. 45 (10) (2019) 12942–12948.
[28] E.R. Hoglund, D.-L. Bao, A. O'Hara, S. Makarem, Z.T. Piontkowski, J.R. Matson, A.K. Yadav, R.C. Haislmaier, R. Engel-Herbert, J.F. Ihlefeld, et al., Emergent interface vibrational structure of oxide superlattices, Nature 601 (7894) (2022) 556–561.
[29] E.R. Hoglund, D.-L. Bao, A. O'Hara, T.W. Pfeifer, M.S.B. Hoque, S. Makarem, J.M. Howe, S.T. Pantelides, P.E. Hopkins, J.A. Hachtel, Direct visualization of localized vibrations at complex grain boundaries, Adv. Mater. (2023) 2208920.
[30] W.G. Fahrenholtz, G.E. Hilmas, Ultra-high temperature ceramics: materials for extreme environments, Scr. Mater. 129 (2017) 94–99.
[31] D. Marshall, B. Cox, P. Kroll, G. Hilmas, W. Fahrenholtz, R. Raj, R. Ritchie, Q. Yang, F. Zok, National hypersonic science center for materials and structures, 2014.
[32] W.G. Fahrenholtz, E.J. Wuchina, W.E. Lee, Y. Zhou, Ultra-high temperature ceramics: materials for extreme environment applications, John Wiley & Sons, 2014.
[33] N.P. Padture, Advanced structural ceramics in aerospace propulsion, Nature Mater. 15 (8) (2016) 804–809.
[34] S. Akrami, P. Edalati, M. Fuji, K. Edalati, High-entropy ceramics: Review of principles, production and applications, Mater. Sci. Eng. R 146 (2021) 100644.
[35] H. Xiang, Y. Xing, F.-z. Dai, H. Wang, L. Su, L. Miao, G. Zhang, Y. Wang, X. Qi, L. Yao, H. Wang, B. Zhao, J. Li, Y. Zhou, High-entropy ceramics: Present status, challenges, and a look forward, J. Adv. Ceram. 10 (3) (2021) 385–441.
[36] H. Kinoshita, S. Otani, S. Kamiyama, H. Amano, I. Akasaki, J. Suda, H. Matsunami, Zirconium diboride (0001) as an electrically conductive lattice-matched substrate for gallium nitride, Japan. J. Appl. Phys. 40 (12A) (2001) L1280.
[37] J.M. Lonergan, W.G. Fahrenholtz, G.E. Hilmas, Zirconium diboride with high thermal conductivity, J. Am. Ceram. Soc. 97 (6) (2014) 1689–1691.
[38] S. Tang, J. Deng, S. Wang, W. Liu, K. Yang, Ablation behaviors of ultra-high temperature ceramic composites, Mater. Sci. Eng. A 465 (1–2) (2007) 1–7.

[39] X. Jin, X. Fan, C. Lu, T. Wang, Advances in oxidation and ablation resistance of high and ultra-high temperature ceramics modified or coated carbon/carbon composites, J. Eur. Ceram. Soc. 38 (1) (2018) 1–28.
[40] S.D. Kasen, Thermal management at hypersonic leading edges, Univ. Va. (2013).
[41] M.A. Maruf, M. Noor-A-Alam, W. Haider, I. Shabib, Enhancing controlled and uniform degradation of Fe by incorporating Mg and Zn aimed for bio-degradable material applications, Mater. Chem. Phys. 285 (2022) 126171.
[42] W.G. Fahrenholtz, G.E. Hilmas, I.G. Talmy, J.A. Zaykoski, Refractory diborides of zirconium and hafnium, J. Am. Ceram. Soc. 90 (5) (2007) 1347–1364.
[43] M. Qin, J. Gild, C. Hu, H. Wang, M.S.B. Hoque, J.L. Braun, T.J. Harrington, P.E. Hopkins, K.S. Vecchio, J. Luo, Dual-phase high-entropy ultra-high temperature ceramics, J. Eur. Ceram. Soc. 40 (15) (2020) 5037–5050.
[44] J.L. Braun, D.H. Olson, J.T. Gaskins, P.E. Hopkins, A steady-state thermoreflectance method to measure thermal conductivity, Rev. Sci. Instrum. 90 (2) (2019) 024905.
[45] D.G. Cahill, Analysis of heat flow in layered structures for time-domain thermoreflectance, Rev. Sci. Instrum. 75 (12) (2004) 5119–5122.
[46] J.P. Feser, J. Liu, D.G. Cahill, Pump-probe measurements of the thermal conductivity tensor for materials lacking in-plane symmetry, Rev. Sci. Instrum. 85 (10) (2014) 104903.
[47] P. Jiang, X. Qian, R. Yang, Tutorial: Time-domain thermoreflectance (TDTR) for thermal property characterization of bulk and thin film materials, J. Appl. Phys. 124 (16) (2018) 161103.
[48] K. Aryana, J.A. Tomko, R. Gao, E.R. Hoglund, T. Mimura, S. Makarem, A. Salanova, M.S.B. Hoque, T.W. Pfeifer, D.H. Olson, et al., Observation of solid-state bidirectional thermal conductivity switching in antiferroelectric lead zirconate (PbZrO3), Nature Commun. 13 (1) (2022) 1573.
[49] W. Parker, R. Jenkins, C. Butler, G. Abbott, Flash method of determining thermal diffusivity, heat capacity, and thermal conductivity, J. Appl. Phys. 32 (9) (1961) 1679–1684.
[50] M.S.B. Hoque, Y.R. Koh, J.L. Braun, A. Mamun, Z. Liu, K. Huynh, M.E. Liao, K. Hussain, Z. Cheng, E.R. Hoglund, D.H. Olson, J.A. Tomko, K. Aryana, R. Galib, J.T. Gaskins, High in-plane thermal conductivity of aluminum nitride thin films, ACS Nano 15 (6) (2021) 9588–9599.
[51] M.S.B. Hoque, Y.R. Koh, K. Aryana, E.R. Hoglund, J.L. Braun, D.H. Olson, J.T. Gaskins, H. Ahmad, M.M.M. Elahi, J.K. Hite, Z.C. Leseman, W.A. Doolittle, P.E. Hopkins, Thermal conductivity measurements of sub-surface buried substrates by steady-state thermoreflectance, Rev. Sci. Instrum. 92 (6) (2021) 064906.
[52] Y.R. Koh, M.S.B. Hoque, H. Ahmad, D.H. Olson, Z. Liu, J. Shi, Y. Wang, K. Huynh, E.R. Hoglund, K. Aryana, J.M. Howe, M.S. Goorsky, S. Graham, T. Luo, J.K. Hite, High thermal conductivity and thermal boundary conductance of homoepitaxially grown gallium nitride (GaN) thin films, Phys. Rev. Mater. 5 (10) (2021) 104604.
[53] G.J. Harrington, G.E. Hilmas, Thermal conductivity of ZrB2 and HfB2, Ultrah. Temp. Ceram. Mater. Extrem. Environ. Appl. (2014) 197–235.
[54] H. Xiang, J. Wang, Y. Zhou, Theoretical predictions on intrinsic lattice thermal conductivity of ZrB2, J. Eur. Ceram. Soc. 39 (10) (2019) 2982–2988.
[55] J.W. Zimmermann, G.E. Hilmas, W.G. Fahrenholtz, R.B. Dinwiddie, W.D. Porter, H. Wang, Thermophysical properties of ZrB2 and ZrB2–SiC ceramics, J. Am. Ceram. Soc. 91 (5) (2008) 1405–1411.
[56] A.D. Stanfield, G.E. Hilmas, W.G. Fahrenholtz, Effects of ti, y, and hf additions on the thermal properties of ZrB2, J. Eur. Ceram. Soc. 40 (12) (2020) 3824–3828.
[57] J.M. Lonergan, D.L. McClane, W.G. Fahrenholtz, G.E. Hilmas, Thermal properties of Hf-doped ZrB2 ceramics, J. Am. Ceram. Soc. 98 (9) (2015) 2689–2691.
[58] C.M. Rost, T. Borman, M.D. Hossain, M. Lim, K.F. Quiambao-Tomko, J.A. Tomko, D.W. Brenner, J.-P. Maria, P.E. Hopkins, Electron and phonon thermal conductivity in high entropy carbides with variable carbon content, Acta Mater. 196 (2020) 231–239.
[59] M. Beekman, D.G. Cahill, Cryst. Res. Technol. 52 (10) (2017) 1700114.
[60] M. Gasch, S. Johnson, J. Marschall, Thermal conductivity characterization of hafnium diboride-based ultra-high-temperature ceramics, J. Am. Ceram. Soc. 91 (5) (2008) 1423–1432.
[61] Y. Touloukian, E. Buyco, Thermophysical properties of matter-the TPRC data series. Volume 5. specific heat-nonmetallic solids, 1970.
[62] J. Justin, A. Jankowiak, Ultra high temperature ceramics: Densification, properties and thermal stability., AerospaceLab (3) (2011) p–1.
[63] R.G. Munro, Material properties of titanium diboride, J. Res. Natl. Inst. Stand. Technol. 105 (5) (2000) 709.
[64] I. Akin, B.C. Ocak, F. Sahin, G. Goller, Effects of SiC and SiC-GNP additions on the mechanical properties and oxidation behavior of NbB2, J. Asian Ceram. Soc. 7 (2) (2019) 170–182.
[65] K. Sairam, J. Sonber, T.C. Murthy, C. Subramanian, R. Fotedar, R. Hubli, Reaction spark plasma sintering of niobium diboride, J. Refract. Met. Hard Mater. 43 (2014) 259–262.
[66] E.W. Neuman, M. Thompson, W.G. Fahrenholtz, G.E. Hilmas, Thermal properties of ZrB2-tib2 solid solutions, J. Eur. Ceram. Soc. 41 (15) (2021) 7434–7441.
[67] L. Zhang, D.A. Pejaković, J. Marschall, M. Gasch, Thermal and electrical transport properties of spark plasma-sintered HfB2 and ZrB2 ceramics, J. Am. Ceram. Soc. 94 (8) (2011) 2562–2570.
[68] T.A. Osswald, G. Menges, Materials Science of Polymers for Engineers, Carl Hanser Verlag GmbH Co KG, 2012.
[69] D.H. Olson, J.T. Gaskins, J.A. Tomko, E.J. Opila, R.A. Golden, G.J. Harrington, A.L. Chamberlain, P.E. Hopkins, Local thermal conductivity measurements to determine the fraction of α-cristobalite in thermally grown oxides for aerospace applications, Scr. Mater. 177 (2020) 214–217.
[70] D.H. Olson, V.A. Avincola, C.G. Parker, J.L. Braun, J.T. Gaskins, J.A. Tomko, E.J. Opila, P.E. Hopkins, Anisotropic thermal conductivity tensor of b-y2si2o7 for orientational control of heat flow on micrometer scales, Acta Mater. 189 (2020) 299–305.
[71] H.-T. Liu, J. Zou, D.-W. Ni, W.-W. Wu, Y.-M. Kan, G.-J. Zhang, Textured and platelet-reinforced ZrB2-based ultra-high-temperature ceramics, Scr. Mater. 65 (1) (2011) 37–40.
[72] Y. Zhang, S.-K. Sun, W.-M. Guo, W. Zhang, L. Xu, J.-H. Yuan, D.-K. Guan, D.-W. Wang, Y. You, H.-T. Lin, Fabrication of textured (Hf0. 2Zr0. 2Ta0. 2Cr0. 2Ti0. 2) B2 high-entropy ceramics, J. Eur. Ceram. Soc. 41 (1) (2021) 1015–1019.
[73] Y. Jee, M.F. Becker, R.M. Walser, Laser-induced damage on single-crystal metal surfaces, J. Opt. Soc. Amer. B 5 (3) (1988) 648–659.
[74] Z. Sun, M. Lenzner, W. Rudolph, Generic incubation law for laser damage and ablation thresholds, J. Appl. Phys. 117 (7) (2015) 073102.
[75] J. Tomko, J.J. Naddeo, R. Jimenez, Y. Tan, M. Steiner, J.M. Fitz-Gerald, D.M. Bubb, S.M. O'Malley, Size and polydispersity trends found in gold nanoparticles synthesized by laser ablation in liquids, Phys. Chem. Chem. Phys. 17 (25) (2015) 16327–16333.
[76] J.A. Tomko, A. Giri, B.F. Donovan, D.M. Bubb, S.M. O'Malley, P.E. Hopkins, Energy confinement and thermal boundary conductance effects on short-pulsed thermal ablation thresholds in thin films, Phys. Rev. B 96 (1) (2017) 014108.
[77] E.G. Gamaly, A.V. Rode, B. Luther-Davies, V.T. Tikhonchuk, Ablation of solids by femtosecond lasers: Ablation mechanism and ablation thresholds for metals and dielectrics, Phys. Plasmas 9 (3) (2002) 949–957.
[78] J.L. Braun, S.W. King, A. Giri, J.T. Gaskins, M. Sato, T. Fujiseki, H. Fujiwara, P.E. Hopkins, Breaking network connectivity leads to ultralow thermal conductivities in fully dense amorphous solids, Appl. Phys. Lett. 109 (19) (2016) 191905.
[79] W.C. Oliver, G.M. Pharr, An improved technique for determining hardness and elastic modulus using load and displacement sensing indentation experiments, J. Mater. Res. 7 (6) (1992) 1564–1583.
[80] Z. Ding, M. Ridley, J. Deijkers, N. Liu, M.S.B. Hoque, J. Gaskins, M. Zebarjadi, P.E. Hopkins, H. Wadley, E. Opila, K. Esfarjani, The thermal and mechanical properties of hafnium orthosilicate: experiments and first-principles calculations, Materialia 12 (2020) 100793.
[81] S.A.A. Shalmani, M. Sobhani, O. Mirzaee, M. Zakeri, Effect of HfB2 and WC additives on the ablation resistance of ZrB2–SiC composite coating manufactured by SPS, Ceram. Int. 46 (16) (2020) 25106–25112.
[82] Y. Zhou, H. Xiang, Z. Feng, Z. Li, General trends in electronic structure, stability, chemical bonding and mechanical properties of ultrahigh temperature ceramics TMB2 (tm=transition metal), J. Mater. Sci. Technol. 31 (3) (2015) 285–294.